PROCEEDINGS OF SPIE

SPIEDigitalLibrary.org/conference-proceedings-of-spie

Investigating the effects of compressional and elastic photoacoustic waves to predict transcranial photoacoustic image quality for guidance of minimally invasive neurosurgeries

Graham, Michelle, Dunne, Reese, Lediju Bell, Muyinatu

Michelle T. Graham, Reese A. Dunne, Muyinatu A. Lediju Bell, "Investigating the effects of compressional and elastic photoacoustic waves to predict transcranial photoacoustic image quality for guidance of minimally invasive neurosurgeries," Proc. SPIE 11631, Advanced Biomedical and Clinical Diagnostic and Surgical Guidance Systems XIX, 116310Q (5 March 2021); doi: 10.1117/12.2579076

SPIE.

Event: SPIE BiOS, 2021, Online Only

Investigating the effects of compressional and elastic photoacoustic waves to predict transcranial photoacoustic image quality for guidance of minimally invasive neurosurgeries

Michelle T. Graham[1], Reese A. Dunne[2], and Muyinatu A. Lediju Bell[1,3,4]

[1]Department of Electrical and Computer Engineering, Johns Hopkins University, Baltimore, MD, USA
[2]Department of Mechanical Engineering, Mississippi State University, Starkville, MS, USA
[3]Department of Biomedical Engineering, Johns Hopkins University, Baltimore, MD, USA
[4]Department of Computer Science, Johns Hopkins University, Baltimore, MD, USA

ABSTRACT

Patient simulations can be a powerful tool to plan placement of photoacoustic imaging components for surgical guidance. We previously used compressional-wave-only simulations to identify optimal acoustic windows for transcranial photoacoustic imaging. Elastic simulations, which include both compressional and shear waves, are expected to more accurately represent the physical transcranial acoustic process. However, elastic simulations are timing-consuming and memory intensive. This paper contains a comparison of compressional and elastic wave simulations to determine which option is more suitable for preoperative surgical planning. Compressional and elastic photoacoustic k-Wave simulations were performed based on a CT volume of a human cadaver head. Photoacoustic sources were placed in the locations of the internal carotid arteries and likely positions of neurosurgical instrument tips. Transducers received signals from three acoustic windows (i.e., the ocular, nasal, and temporal regions). Target visibility, image-based target size estimates, and target-to-instrument distances were measured using the generalized contrast-to-noise ratio, resolution, and relative source distances, respectively, for each simulation method. The generalized contrast-to-noise ratio and resolution measurements were equivalent between compressional and elastic simulations. Relative source distance measurements were within 0.1 mm of the true distances. These results indicate that it is sufficient to utilize the less time-consuming, less memory-intensive compressional wave simulations for presurgical planning.

1. INTRODUCTION

The endonasal transsphenoidal approach to pituitary tumor resection is a minimally invasive technique that requires insertion of surgical instruments through the nose to remove sphenoid bone and underlying pituitary tumors.[1] Although the procedure is generally safe,[2] morbidity and mortality rates rise to 14-23% and 24-26%, respectively, if iatrogenic injury to the internal carotid arteries (ICAs) occurs.[3–5] Current intraoperative guidance techniques, such as stereotactic guidance and endoscopy, enable monitoring of the ICAs in close proximity to the surgical site, however, they suffer from two primary limitations. First, stereotactic guidance is subject to registration errors which can become increasingly large as patient anatomy is disrupted during surgery and deviates from the anatomy in preoperative x-ray computed tomography (CT) or magnetic resonance (MR) images. Second, endoscopy is unable to identify the ICAs when they are obscured by bone or other tissues in the operative path. Our group is investigating the use of transcranial photoacoustic imaging as an intraoperative imaging technique for real-time visualization of the ICAs to address these two limitations.[6–12]

To achieve photoacoustic imaging for guidance of endonasal transsphenoidal surgery, we propose the insertion of light-transmitting fiber optic devices in the nasal cavity, similar to other surgical tools.[6–12] This light source will then excite the hemoglobin within the ICAs, converting the absorbed optical energy to acoustic energy that is received by an externally placed ultrasound receiver. The external ultrasound receiver placement results in a transcranial photoacoustic imaging scenario, which is challenged by acoustic interactions with bone and is known to degrade image quality.[13–15] Previous work from our group developed and demonstrated a simulation

Advanced Biomedical and Clinical Diagnostic and Surgical Guidance Systems XIX, edited by Caroline Boudoux, James W. Tunnell, Proc. of SPIE Vol. 11631, 116310Q · © 2021 SPIE
CCC code: 1605-7422/21/$21 · doi: 10.1117/12.2579076

method to identify naturally occurring acoustic windows in the adult human skull in order to minimize acoustic interactions with bone and to provide high-contrast photoacoustic images of the ICAs.[10,11] We demonstrated that patient-specific simulations have the potential to enable preoperative planning to determine appropriate placement of imaging system components, using compressional-wave-only simulations.[10,11] However, the shear waves known to propagate within dense media such as bone were excluded from our initial demonstrations.

As an alternative to compressional-wave-only simulations, elastic simulations, which include both compressional and shear waves, are expected to more accurately represent the physical acoustic process. However, elastic wave simulations, such as the k-Wave elastic simulations based on the classical Kelvin-Voigt absorption model, are time-consuming and memory-intensive.[16] Time and memory costs reduce the ease and likelihood of clinical translation. This paper presents a comparison of compressional and elastic photoacoustic k-Wave simulations in order to investigate which simulation type (i.e., compressional or elastic) is required for preoperative surgical planning.

2. METHODS

Three-dimensional photoacoustic k-Wave[17,18] simulations were performed after converting the CT volume of a human cadaver skull into heterogeneous, volumetric maps of corresponding density, compressional and shear wave sound speeds, and compressional and shear wave absorption prefactors. Fig. 1 shows an example axial slice from the CT volume of a human cadaver skull. Homogeneous volumes were additionally modeled as the average density, sound speed, and absorption values of brain tissue in order to provide baseline photoacoustic images that do not contain heterogeneous tissue effects, such as aberration, attenuation, and reverberation. The simulated tissue properties for the heterogeneous and homogeneous cases are reported in Table 1. The computational grid was defined with a symmetric voxel size of 0.3 mm x 0.3 mm x 0.3 mm. Acoustic wave propagation was simulated with a time increment of 1.12^{-8} seconds on a NVIDIA Quadro RTX 6000 GPU.

Phased array ultrasound transducers with 0.3 mm pitch, 13.5 mm height, 0 mm kerf, and 64 elements were positioned to receive transcranial photoacoustic signals from three acoustic windows: (1) the left ocular cavity, (2) the left temple region, and (3) nasal cavity (see Fig. 1). A spherical photoacoustic source with a diameter of 0.3 mm (i.e., a point source) or 4 mm (i.e., the diameter of a typical adult carotid artery) was placed in the location of the left carotid artery (LCA), as shown in Fig. 1. To investigate photoacoustic image characteristics when the tip of a surgical instrument is in the imaging plane, a second 0.3 mm-diameter spherical photoacoustic source was positioned within the surgical site at distances of 2-11 mm from the LCA target. The distances of the LCA source relative to the center of the transducers located on the ocular, nasal, and temple regions were 7.40 mm, 8.02, and 5.03 mm, respectively. Received transducer channel data were bandpass filtered to contain -6 dB

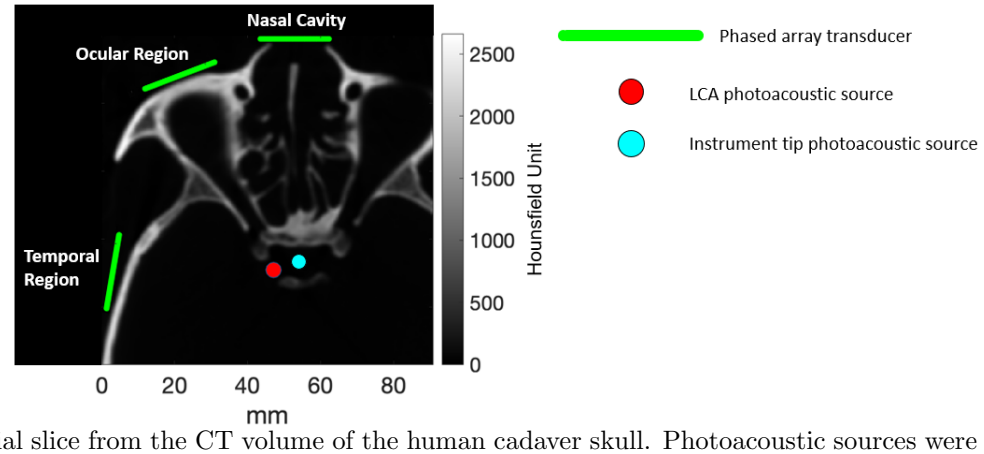

Figure 1: Axial slice from the CT volume of the human cadaver skull. Photoacoustic sources were placed within the left internal carotid artery (LCA) and at distances of 2-11 mm from the LCA to represent a the tip of a surgical instrument (a distance of 5.94 mm is shown). Green lines illustrate locations of independently placed ultrasound transducers.

Table 1: Simulated tissue properties of the homogeneous and heterogeneous volumetric maps.[17,19–24] The two shear wave properties of sound speed in brain and absorption power law prefactors in bone and brain are not explicitly known. However, these properties can be estimated as approximately half the corresponding compressional speed of sound and approximately double the corresponding compressional absorption power law prefactor.[23,25]

		Speed of Sound (m/s)	**Absorption Power Law Prefactor[18,26] (dB MHz$^{1.18}$/cm)**	**Density (kg/m^3)**
Bone	Compression	1300 - 3492[17,19]	1.36 - 2.50[21]	812 - 2770[17,20]
	Shear	650 - 1746[23]	2.71 - 5.00*	
Brain	Compression	1519[24]	0.21[21,22]	1045[24]
	Shear	800*	0.75*	

*Estimated shear wave values

frequencies in the range 1-5 MHz. Randomly distributed Gaussian noise was added to the received channel data obtained with the transducer located in the temporal region in order to model the electronic noise of an imaging system, resulting in a 15 dB channel signal-to-noise ratio (SNR). The same noise distribution was then added to the received channel data obtained with the remaining transducer locations (i.e., nasal and temple regions) in order to simulate the same noise floor for the three transducer locations, each viewing photoacoustic signals of the same 4 mm target.

Photoacoustic delay-and-sum (DAS) images were generated from the filtered channel data with additive noise. DAS image quality (i.e., resolution, target visibility, and target detectability) was measured for each transducer location. Resolution was assessed by calculating the area of the -6 dB contour of the point spread function (PSF), measured from images of the point target. Target visibility was assessed using images of the the 4 mm-diameter LCA target to measure contrast, signal-to-noise ratio (SNR), and contrast-to-noise ratio (CNR), while target detectability was assessed using the generalized contrast-to-noise ratio (gCNR).[27,28] These image quality metrics are defined as follows:

$$\text{Contrast} = 20\log_{10}\left(\frac{\mu_t}{\mu_b}\right), \tag{1}$$

$$\text{SNR} = \frac{\mu_t}{\sigma_b}, \tag{2}$$

$$\text{CNR} = \frac{|\mu_t - \mu_b|}{\sqrt{\sigma_t^2 + \sigma_b^2}}, \tag{3}$$

$$\text{gCNR} = 1 - \sum_{k=0}^{N-1} \min\{h_i(x_k), h_o(x_k)\}, \tag{4}$$

where μ_t and μ_b are the means, σ_t and σ_b are the standard deviations, and h_t and h_b are the histograms of the signal amplitudes within ellipsoidal regions of interest (ROIs) placed within the photoacoustic target (denoted by subscript t) or within the background of the photoacoustic image (denoted by subscript b), N is the number of bins in the histogram, and k is the index of the bin. A total of $N = 145$ bins were used to create the histograms for the gCNR measurements. The target ROI was centered on the brightest pixel in the image and the background ROI was centered 20 mm above the target ROI.

Target-to-instrument tip distances were measured from DAS photoacoustic images of the LCA and the instrument tip, calculated as the Euclidean distance between the brightest image pixel from each source. The distance error was calculated as the absolute difference between the measured target-to-instrument tip distance and the known target-to-instrument distance. Considering that the ICAs typically lie within 1 to 7 mm of the surgical site,[29,30] a distance error <1 mm was considered to be sufficient for the proposed technology.

Table 2: Comparison of execution times and memory usage for the compressional and elastic k-Wave simulations.

	Time (minutes)		Memory (GB)	
	Compressional	Elastic	Compressional	Elastic
Ocular	9.26	43.73	3.02	8.10
Nasal	10.24	47.79	3.22	8.65
Temporal	10.65	46.80	3.75	10.13
Mean	10.05	45.85	3.33	8.96

3. RESULTS

Table 2 compares the execution time and memory usage of the compressional and elastic simulations, performed with the three independently placed transducers illustrated in Fig. 1. The last row of this table reports the mean time and memory usage across the three simulations to demonstrate that elastic simulations required approximately 4.6x more time and 2.7x more memory than compressional simulations.

Fig. 2(a) shows simulated photoacoustic images generated from the heterogeneous simulations of the 4 mm-diameter LCA source. The shape, location, and visibility of the targets generally agree between the compressional and elastic simulation pairs for each transducer location. Fig. 2(b) quantifies the target visibility and detectability

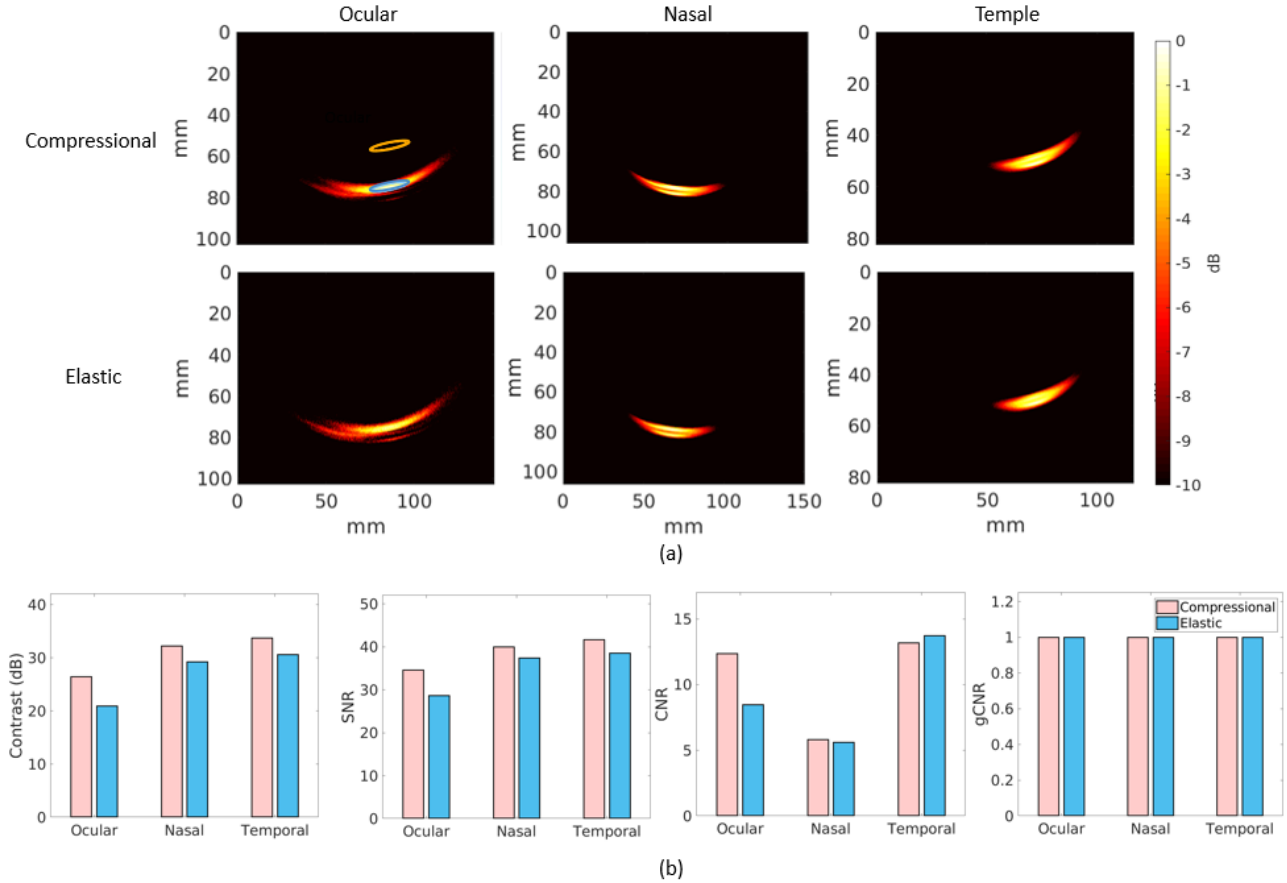

Figure 2: (a) Simulated photoacoustic images of the left internal carotid artery obtained with the ocular, nasal, and temporal acoustic windows, from left to right respectively. The top and bottoms rows show compressional and elastic simulation results, respectively. The target and background ellipsoidal regions of interest are outlined in blue and orange, respectively. Images are displayed with 10 dB dynamic range. (b) Corresponding contrast, signal-to-noise ratio (SNR), contrast-to-noise ratio (CNR), and generalized contrast-to-noise ratio (gCNR)[27,28] measurements.

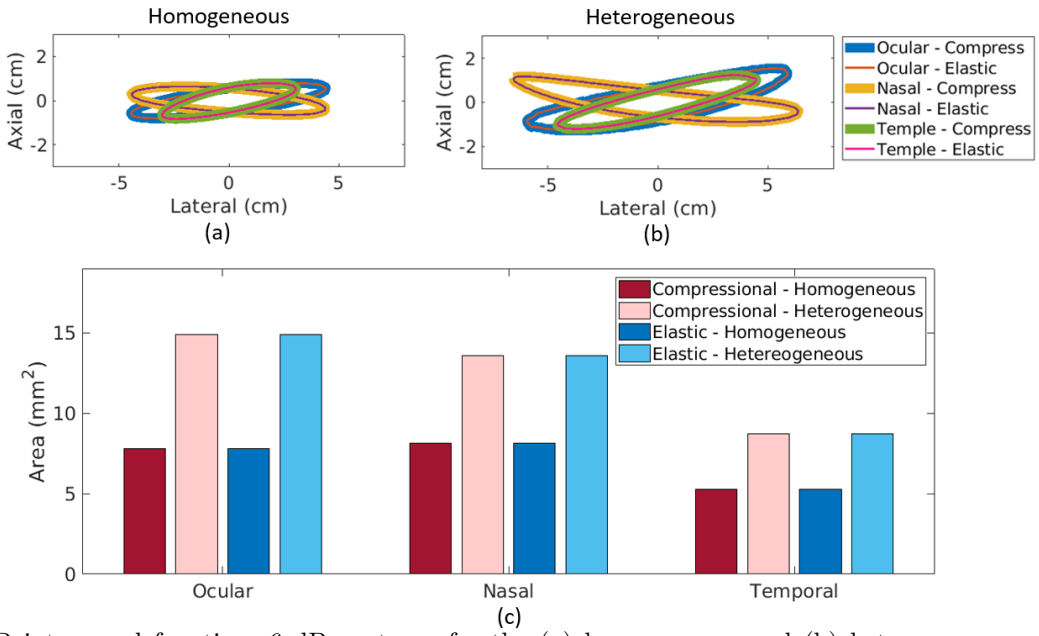

Figure 3: Point spread function -6 dB contours for the (a) homogeneous and (b) heterogeneous point target simulations. (c) Corresponding areas of the point spread function -6 dB contours. Homogeneous simulation measurements provide baseline resolution measurements without the negative effects of tissue heterogeneity.

of the heterogeneous simulated images displayed in Fig. 2(a). There were minimal differences in contrast, SNR and CNR measurements, and the gCNR measurements were equivalent. Therefore, the visibility and detectability of these photoacoustic image targets is ranges from similar to equivalent for compressional and elastic wave simulations.[28]

Figs. 3(a) and 3(b) show the -6 dB contours of the point target images from the homogeneous and heterogenous simulations, respectively. Fig. 3(c) shows the calculated areas of the contours. The contour areas of the baseline

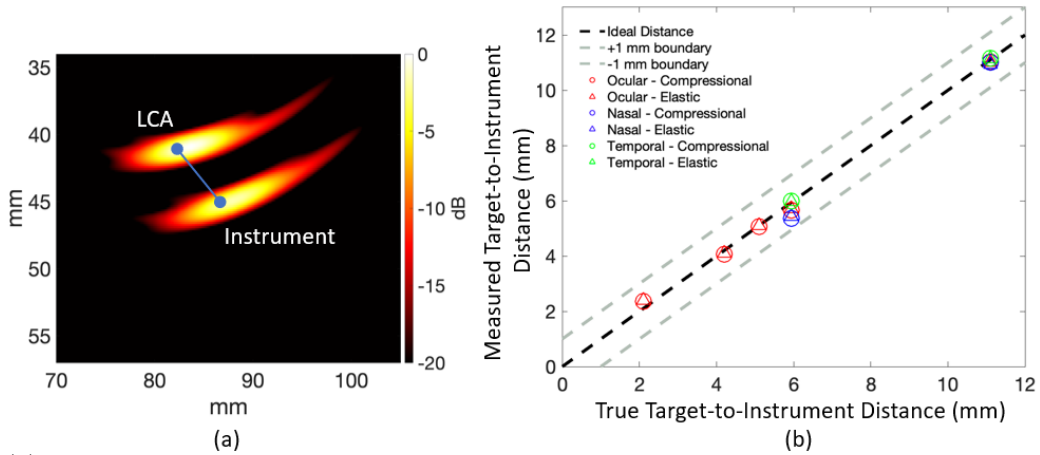

Figure 4: (a) Heterogeneous simulated photoacoustic images of the two sources representing the LCA and instrument tip, obtained with the temporal acoustic window at a relative distance of 5.94 mm. The target-to-instrument distance is the length of the line between the source centers in the image. (b) Comparison of measured target-to-instrument distances as a function of the true target-to-instrument distances for compressional (○) and elastic (△) measurements in the ocular, nasal, and temporal acoustic windows. The ideal 1:1 relationship is shown as the dashed black line, with ± 1 mm boundaries indicated by the dashed gray lines.

homogeneous simulated images were 7.80 mm^2, 8.13 mm^2, and 5.28 mm^2 for the ocular, nasal, and temple acoustic windows, respectively, for both compressional and elastic simulations. The areas of the corresponding simulated images obtained with the heterogeneous skull model were 14.90 mm^2, 13.56 mm^2, and 8.73 mm^2, respectively. Therefore, the resolution of these photoacoustic images is equivalent for compressional and elastic wave simulations.

Fig. 4(a) shows an annotated photoacoustic image from a heterogeneous simulation of the LCA and a surgical instrument tip, obtained with the temporal acoustic window. The ground truth target-to-instrument distance is 5.94 mm and the measured target-to-instrument distance is 6.00 mm in this image. Fig. 4(b) displays image-based measurements of multiple target-to-instrument distances as a function of ground truth distances. The largest distance error between measurements and ground truth was obtained with the nasal cavity images, measuring 0.57 mm and 0.51 mm for the compressional and elastic wave simulations, respectively. The errors for the ocular and temporal regions ranged 0.06-0.28 mm and 0.03-0.22 mm for the compressional and elastic simulations, respectively. When comparing the target-to-instrument distance errors between the compressional and elastic simulations, the differences in errors were 0.06, 0.06, and 0.03 for the ocular, nasal, and temporal regions, respectively. Therefore, relative target-to-instrument distances can be measured with sub-millimeter accuracy from both compressional and elastic wave simulations.

4. DISCUSSION

This paper describes our investigations of elastic wave simulations as a potential method for presurgical planning of transducer placement during transcranial photoacoustic image-guided neurosurgery. In particular, comparative differences in image quality (i.e., target visibility, target detectability, and target size estimation) and target-to-instrument tip distances between a critical blood vessel and surgical instrument tip were assessed with photoacoustic images generated from compressional and elastic transcranial simulations. Qualitatively and quantitatively, target visibility and detectability were relatively similar between the compressional and elastic simulations for the three acoustic windows tested (see Fig. 2). In addition, image resolution was equivalent between compressional and elastic simulations for the three acoustic windows tested (see Fig. 3). Lastly, both compressional and elastic simulations measured target-to-instrument tip distances within 1 mm accuracy (see Fig. 4).

Our results indicate that it is sufficient to utilize the less time-consuming, less memory-intensive compressional simulations for presurgical planning. A shorter simulation time makes simulations easier to adapt into the current presurgical workflow. Reduced computational memory places less strain on computational resource requirements for presurgical simulations. Overall, this work advances simulation-based photoacoustic-guided surgery towards clinical translation. In particular, this presurgical planning step has the potential to rapidly identify patient-specific optimal transducer locations for incorporation into the surgical plan.

Presurgical identification of optimal photoacoustic imaging system component locations offers three primary benefits. First, this presurgical identification would eliminate wasting valuable operating room time to search for and find a suitable transducer location, thereby reducing the time the patient is under anesthesia, the total procedure duration, and the medical cost. The second benefit is removal of the potential barrier that the surgeon may be unable to identify a viable transducer location and therefore unable to use photoacoustic image-guidance during the procedure. The third benefit is identification of transducer locations which would minimize image quality degradation from the presence of bone and thereby produce photoacoustic images of the ICAs with the best image quality possible for the patient.

5. CONCLUSION

The work presented in this paper is the first to reveal that the less time-consuming and less memory-intensive compressional k-Wave simulations are sufficient for identification of optimal transducer locations for transcranial photoacoustic-guided surgery. This assessment is based on target visibility and detectability (e.g., target contrast, SNR, CNR, and gCNR), target size estimates (i.e., point spread function -6 dB contour area), and relative source-to-instrument distance producing similar or identical quantatitive measurements for compressional and elastic simulations. These results have multiple implications for reducing barriers for clinical translation of simulation-based photoacoustic-guided surgery.

ACKNOWLEDGMENTS

This work was supported by the Computational Sensing and Medical Robotics Research Experience for Undergraduates Program (Grant No. EEC-1852155), NIH Grant No. R00EB018994, NSF CAREER Award Grant No. ECCS 1751522, and the NSF Graduate Research Fellowship Program (Grant No. DGE1746891).

REFERENCES

[1] Cappabianca, P., Cavallo, L. M., and de Divitiis, E., "Endoscopic endonasal transsphenoidal surgery," *Neurosurgery* **55**, 933–941 (2004).

[2] Ciric, I., Ragin, A., Baumgartner, C., and Pierce, D., "Complications of transsphenoidal surgery: Results of a national survey, review of the literature, and personal experience," *Neurosurgery* **40**(2), 225–237 (1997).

[3] Perry, M. O., Snyder, W. H., and Thal, E. R., "Carotid artery injuries caused by blunt trauma," *Annals of Surgery* **192**(1), 74–77 (1980).

[4] Raymond, J., Hardy, J., Czepko, R., and Roy, D., "Arterial injuries in transsphenoidal surgery for pituitary adenoma; the role of angiography and endovascular treatment," *American Journal of Neuroradiology* **18**(4), 655–665 (1997).

[5] Valentine, R. and Wormald, P.-J., "Carotid artery injury after endonasal surgery," *Otolaryngologic Clinics of North America* **44**(5), 1059–1079 (2011).

[6] Bell, M. A. L., Ostrowski, A. K., Li, K., Kazanzides, P., and Boctor, E. M., "Localization of transcranial targets for photoacoustic-guided endonasal surgeries," *Photoacoustics* **3**(2), 78–87 (2015).

[7] Bell, M. A. L., Ostrowski, A. K., Li, K., Kazanzides, P., and Boctor, E. M., "Quantifying bone thickness, light transmission, and contrast interrelationships in transcranial photoacoustic imaging," in [*Proceedings of SPIE, Photons Plus Ultrasound: Imaging and Sensing*], **9323** (2015).

[8] Bell, M. A. L., Dagle, A. B., Kazanzides, P., and Boctor, E. M., "Experimental assessment of energy requirements and tool tip visibility for photoacoustic-guided endonasal surgery," in [*Proceedings of SPIE, Photons Plus Ultrasound: Imaging and Sensing*], **9708**, 97080D (2016).

[9] Bell, M. A. L., Ostrowski, A. K., Kazanzides, P., and Boctor, E. M., "Feasibility of transcranial photoacoustic imaging for interventional guidance of endonasal surgeries," in [*Proceedings of SPIE, Photons Plus Ultrasound: Imaging and Sensing*], **8943**(894307) (2014).

[10] Graham, M. T., Huang, J., Creighton, F., and Bell, M. A. L., "Simulations and human cadaver head studies to identify optimal acoustic receiver locations for minimally invasive photoacoustic-guided neurosurgery," *Photoacoustics* , 100183 (2020).

[11] Graham, M. T., Creighton, F. X., and Bell, M. A. L., "Investigation of acoustic windows for photoacoustic imaging of intracranial blood vessels," in [*2020 IEEE International Ultrasonics Symposium (IUS)*], 1–4, IEEE (2020).

[12] Lediju Bell, M. A., "Photoacoustic imaging for surgical guidance: Principles, applications, and outlook," *Journal of Applied Physics* **128**(6), 060904 (2020).

[13] Kneipp, M., Turner, J., Estrada, H., Rebling, J., Shoham, S., and Razansky, D., "Effects of the murine skull in optoacoustic brain microscopy," *Journal of Biophotonics* **9**(1-2), 117–123 (2016).

[14] Pinton, G., Aubry, J.-F., Bossy, E., Muller, M., Pernot, M., and Tanter, M., "Attenuation, scattering, and absorption of ultrasound in the skull bone," *Medical Physics* **39**(1), 299–307 (2012).

[15] Estrada, H., Rebling, J., Turner, J., and Razansky, D., "Broadband acoustic properties of a murine skull," *Physics in Medicine & Biology* **61**(5), 1932 (2016).

[16] Firouzi, K., Cox, B., Treeby, B., and Saffari, N., "A first-order k-space model for elastic wave propagation in heterogeneous media," *The Journal of the Acoustical Society of America* **132**(3), 1271–1283 (2012).

[17] Treeby, B. E. and Cox, B. T., "k-Wave: MATLAB toolbox for the simulation and reconstruction of photoacoustic wave fields," *Journal of Biomedical Optics* **15**(2), 021314 (2010).

[18] Treeby, B. E., Cox, B. T., and Jaros, J., *A MATLAB toolbox for the time domain simulation of acoustic wave field, User manual, (2016) Manual Version 1.1, Toolbox Release 1.1.*

[19] Mast, T. D., "Empirical relationships between acoustic parameters in human soft tissues," *Acoustics Research Letters Online* **1**(2), 37–42 (2000).

[20] Schneider, U., Pedroni, E., and Lomax, A., "The calibration of ct hounsfield units for radiotherapy treatment planning," *Physics in Medicine & Biology* **41**(1), 111 (1996).
[21] Duck, F. A., [*Physical properties of tissues: a comprehensive reference book*], Academic press (2013).
[22] White, D., Curry, G., and Stevenson, R., "The acoustic characteristics of the skull," *Ultrasound in medicine & biology* **4**(3), 225–252 (1978).
[23] White, P. J., Clement, G. T., and Hynynen, K., "Longitudinal and shear mode ultrasound propagation in human skull bone," *Ultrasound in medicine & biology* **32**(7), 1085–1096 (2006).
[24] Lloyd, B. A., "Tissue properties," *IT'IS Foundation* (2020).
[25] Clement, G. T., White, P. J., and Hynynen, K., "Enhanced ultrasound transmission through the human skull using shear mode conversion," *The Journal of the Acoustical Society of America* **115**(3), 1356–1364 (2004).
[26] Treeby, B. E. and Cox, B. T., "Modeling power law absorption and dispersion for acoustic propagation using the fractional laplacian," *The Journal of the Acoustical Society of America* **127**(5), 2741–2748 (2010).
[27] Rodriguez-Molares, A., Rindal, O. M. H., D'hooge, J., Måsøy, S.-E., Austeng, A., Bell, M. A. L., and Torp, H., "The generalized contrast-to-noise ratio: a formal definition for lesion detectability," *IEEE Transactions on Ultrasonics, Ferroelectrics, and Frequency Control* **67**(4), 745–759 (2019).
[28] Kempski, K. M., Graham, M. T., Gubbi, M. R., Palmer, T., and Bell, M. A. L., "Application of the generalized contrast-to-noise ratio to assess photoacoustic image quality," *Biomedical Optics Express* **11**(7), 3684–3698 (2020).
[29] Isolan, G. R., de Aguiar, P. H. P., Laws, E. R., Strapasson, A. C. P., and Piltcher, O., "The implications of microsurgical anatomy for surgical approaches to the sellar region," *Pituitary* **12**(4), 360–367 (2009).
[30] Dusick, J. R., Esposito, F., Malkasian, D., and Kelly, D. F., "Avoidance of carotid artery injuries in transsphenoidal surgery with the doppler probe and micro-hook blades," *Operative Neurosurgery* **60**(suppl_4), ONS–322 (2007).